

www.acsnano.org

A 3D Plasmonic Antenna-Reactor for Nanoscale Thermal Hotspots and Gradients

Pratiksha D. Dongare, $^{\nabla}$ Yage Zhao, $^{\nabla}$ David Renard, $^{\nabla}$ Jian Yang, Oara Neumann, Jordin Metz, Lin Yuan, Alessandro Alabastri, * Peter Nordlander, * and Naomi J. Halas *



Cite This: ACS Nano 2021, 15, 8761-8769



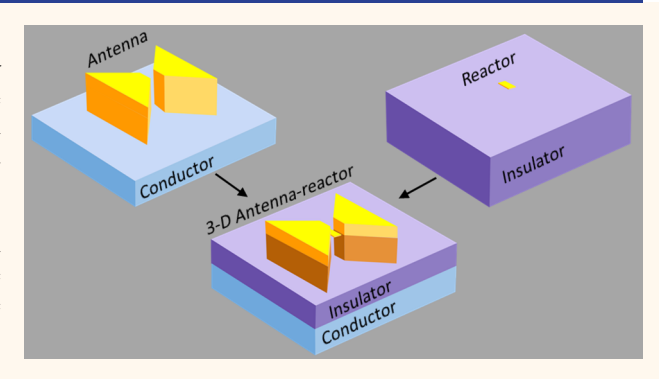
ACCESS

III Metrics & More

Article Recommendations

Supporting Information

ABSTRACT: Plasmonic nanoantennas focus light below the diffraction limit, creating strong field enhancements, typically within a nanoscale junction. Placing a nanostructure within the junction can greatly enhance the nanostructure's innate optical absorption, resulting in intense photothermal heating that could ultimately compromise both the nanostructure and the nanoantenna. Here, we demonstrate a three-dimensional "antennareactor" geometry that results in large nanoscale thermal gradients, inducing large local temperature increases in the confined nanostructure reactor while minimizing the temperature increase of the surrounding antenna. The nanostructure is supported on an insulating substrate within the antenna gap, while the antenna maintains direct contact with an underlying



thermal conductor. Elevated local temperatures are quantified, and high local temperature gradients that thermally reshape only the internal reactor element within each antenna-reactor structure are observed. We also show that high local temperature increases of nominally 200 °C are achievable within antenna-reactors patterned into large extended arrays. This simple strategy can facilitate standoff optical generation of high-temperature hotspots, which may be useful in applications such as small-volume, high-throughput chemical processes, where reaction efficiencies depend exponentially on local temperature.

KEYWORDS: plasmons, hotspots, absorption, light focusing, gradient

trongly localized photothermal effects have gained steadily increasing interest due to their wide range of applications, such as biosensing, chemical catalysis, localized photothermal therapy, and solar thermal energy harvesting. 1-4 Plasmonic nanostructures far smaller than the wavelength of incident resonant light can efficiently absorb that light and act as highly effective nanoscale photothermal transducers. Increasing the size of the nanostructure increases its scattering cross section, making it more effective as a far-field nanoscale antenna, enhancing the optical near field. 5-7 In the latter case, heat dissipation is generally regarded as an unwanted side effect that can limit the optical performance of nanostructures and may lead to their reshaping or even melting when high local temperatures are achieved. Recently, the antenna-reactor (A-R) concept⁸ has been introduced: a combination of nanostructures where nanoscale optical "antennas", acting as lenses, amplify the interaction between light and "reactor" nanostructures, which in isolation would be unable to interact with the incident optical field efficiently. For example, the A-R concept has been extremely practical and effective when the reactor nanostructure can catalyze a chemical

reaction, where the addition of the antenna serves to convert it from a thermocatalyst to a hot carrier-driven photocatalyst. In principle, however, the A-R concept is far more general and can be used to amplify a wide range of other processes. What makes A-R systems particularly useful is their capability to capture electromagnetic energy from larger length scales and focus it within the reactor's nanoscale volume, where that energy can be utilized for various applications. Besides reradiation and emission control, concentrated electromagnetic fields can generate mechanical forces, excite hot carriers, generate high harmonics, location induce phase changes, location and dissipate heat. However, while elevated reactor temperatures may be desirable to drive localized thermal processes, it is also important

Received: February 3, 2021 Accepted: April 16, 2021 Published: April 26, 2021





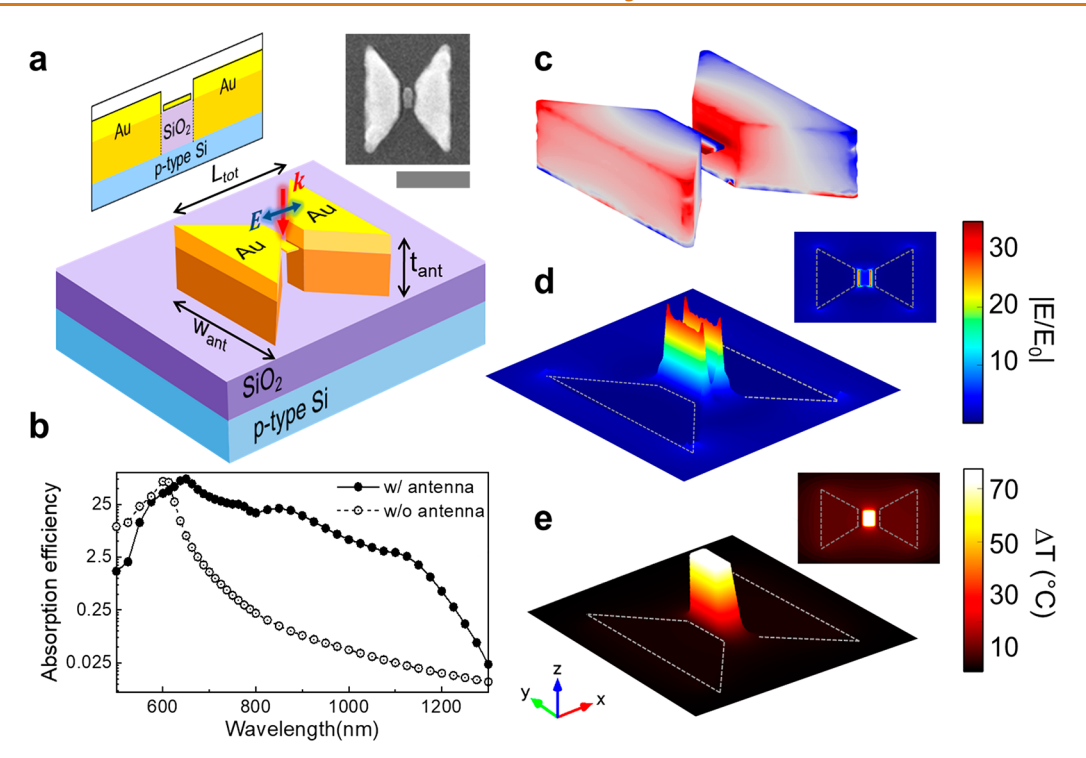


Figure 1. High-temperature gradient generation with increased absorption in the reactor from field enhancement from antenna supported on a heat sink. (a) Top and side view of the three-dimensional schematic representation of the A-R structure showing the bowtie shaped antennas in direct contact with the underlying heat sink (p-type doped Si) and the nanorod reactor supported by an insulating silica layer. The incident light is polarized perpendicular to the bowtie gap. Scanning electron microscope image of the A-R device optimized for 785 nm excitation (scale bar = 300 nm). (b) The absorption efficiency of the reactor with antenna (solid black line with solid circles), without antenna (empty circles). (c) Charge distribution in the A-R structure at 785 nm. (d) Field enhancement in the plane of the structure at 785 nm. (e) Calculated temperature increase distribution in the plane of an individual structure illuminated with an intensity of 435 kW/cm².

that elevated temperatures not compromise the antenna itself. In large arrays, collective thermal effects tend to homogenize the temperature distribution over extended areas, reducing or eliminating nanoscale thermal gradients. ¹⁶ In this work, we demonstrate the presence of large temperature gradients in gold A-R systems by selectively melting the reactor thanks to its enhanced absorption provided by the antenna's optical field enhancement. Additionally, we show how our A-R design can be extended to refractory reactor materials (*e.g.*, tungsten) to avoid melting and therefore potentially catalyze target chemical reactions.

The challenge of creating nanoscale thermal hotspots was initially addressed theoretically, by calculating the local heating that arises in arrangements of nanostructures that support Fano resonances. A Figure of Merit was defined within these studies, providing a metric for the evaluation of nanoscale heating and thermal gradients under various excitation conditions. Early experimental work was limited to planar arrangements of nanostructures, specifically nanorod dimers, where, although localized heating was indirectly demonstrated, its magnitude remained unquantified. 19

Here, we demonstrate an A-R nanostructure complex designed to generate large local thermal hotspots and nanoscale thermal gradients, minimizing antenna overheating and exhibiting elevated local temperatures at the reactor sites over extended areas. The complex consists of a carefully tuned Au bowtie nanoantenna and a small Au nanorod reactor fabricated within its junction. Metallic bowties or alternative plasmonic material 20,21 nanostructures can act as antennas for coupling with propagating fields, localizing electromagnetic energy. 22 In

the past decade, bowties or related geometries²³ have been engineered for multiple applications, including optical tweezers, ²⁴ gas-sensing, ²⁵ optical trapping, ²⁶ and even magnetic data storage²⁷ or audio recording. ²⁸ In our bowtie structure, using the same metal for both antenna and reactor enables us to establish that the temperature differences achieved between the two structures are due to the specific nanoscale geometry, not to differences in thermal conductivities between two different metals (although this same design strategy would also achieve nanoscale thermal gradients using antenna and reactors of different compositions). In our design, the antenna is in direct contact with an underlying thermal conductor (p-type Si) for passive cooling and the reactor is supported on an insulator (silica) to maintain a substantial degree of thermal isolation. The sustained passive cooling of the antenna as it focuses light into the thermally isolated reactor enables reliable long-term operation. The combination of insulated reactors and thermally short-circuited antennas generates a strong thermal transport imbalance along the vertical, z, direction, perpendicular to the substrate. The resulting 3D assembly exhibits a heat transfer asymmetry that induces large temperature increases in the reactor while favoring the cooling of the nearby antenna. A similar approach was previously adopted to enhance infrared absorption in polymer molecules²⁹ and generate large thermal gradients using high-aspect ratio rod-like antennas. 40 Here, we demonstrate how a custom A-R configuration allows exceptional light absorption and temperature increase within a reactor otherwise unable to dissipate heat and accumulate thermal energy. We verified localized temperature gradients at reactor sites in two ways: First, by monitoring the local temperature

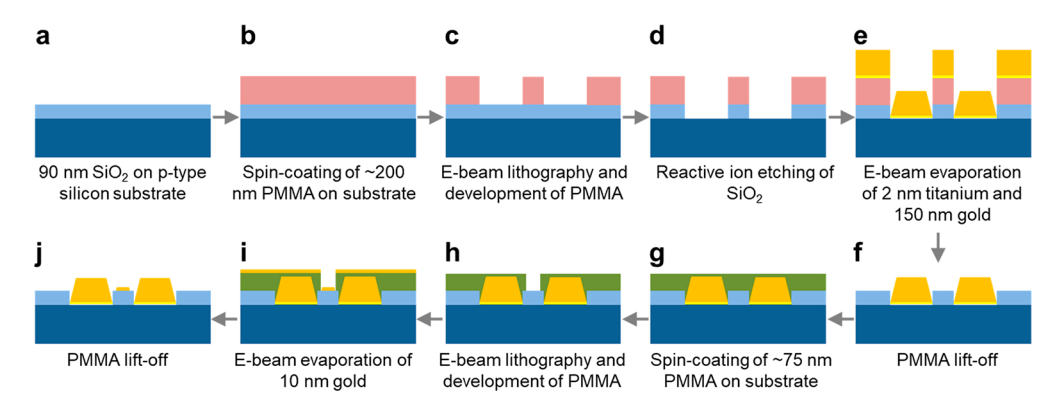


Figure 2. Fabrication of three-dimensional A-R structure. (a) The p-type doped Si substrate has a 90 nm thermal oxide coating. (b) The substrate is spin-coated with \sim 200 nm thick layer of PMMA. (c) The bowtie structures are written with e-beam lithography, and the exposed PMMA is developed in 1:3 MIBK:IPA. (d) Reactive ion etching with CHF $_3$ and O $_2$ helps remove the underlying silica layer in the developed gaps to expose underlying p-type Si. (e) 2 nm titanium and 150 nm Au are e-beam evaporated on top of the exposed Si layer. (f) Lift-off of extra Au in 1-methyl-2-pyrrolidinone leads to well-defined bowtie structures. (g) Layer of \sim 75 nm thick PMMA is spin-coated. (h) E-beam lithography patterns the reactors in the gaps between the bowtie antennas the exposed structures are developed. (i) 10 nm Au is evaporated on top of exposed silica. (j) Extra Au is removed to obtain final three-dimensional A-R structures.

through the Stokes—anti-Stokes ratio of the surface-enhanced Raman scattering (SERS) signal from p-mercaptobenzoic acid (pMBA) molecules adsorbed onto the reactor site within a single A-R. Second, by observing selective reactor reshaping at higher incident light intensities in illuminated A-R arrays. We obtain temperature gradients up to 1.9×10^9 K/m for the A-R system, compared to $\sim 9.3 \times 10^7$ K/m for reactor-only structures under a fixed input illumination intensity (~ 500 kW/cm²). This corresponds to a nanoscale thermal gradient FOM of more than 20, which is significantly higher than the 2.5 obtained in the original theoretical study of a trimer for the same separation (see Supporting Information for specific details). ¹⁸

RESULTS/DISCUSSION

A schematic of the three-dimensional nanostructure complex is shown in Figure 1a, along with a scanning electron microscope image of the fabricated complex (see Figure S1, for all detailed dimensions). Two A-R complexes were fabricated, one (of overall dimensions 408 nm × 340 nm) optimized for 785 nm wavelength incident light for the SERS studies, the other (415 nm × 330 nm) for 808 nm wavelength incident light for highintensity studies (Figure S3). We optimized the physical dimensions of these two A-R structures for maximal reactor absorption enhancements provided by the respective antennas (shown in Figures S4 and S5). Each bowtie antenna had a 120 nm × 40 nm nanorod "reactor" fabricated within its junction. The aspect ratio of the nanorod was specifically chosen so that the nanorod transverse mode is detuned (600 nm) from the illumination wavelengths. A cross-sectional view of the nanostructure is also shown in Figure 1a. The antenna was deposited directly onto a Si substrate, with a height of 150 nm. The nanorod was deposited instead on a silica layer of 90 nm height within the junction of the bowtie antenna. The optical absorption of the reactor alone has a peak at 600 nm wavelength (Figure 1b, dashed black line with hollow circles), while the absorption spectrum of the A-R is significantly broader due to the coupling of the relatively narrow reactor absorption with the broader field enhancement of the antenna (Figure 1b solid black line with solid circles). It should be emphasized that the reactor absorption peak is not relevant (in fact, we detuned our optical response on purpose) since the main goal of our A-R system is to achieve absorption enhancement (due to the antenna) in

reactors with otherwise limited absorption efficiency in the same spectral region. In our case, the relatively broad antenna nearfield enhancement (Figures S4 and S5) provides an increased absorption over a wide spectral range. However, the same concept can be applied to other optical nanostructures featuring sharp resonances that would induce large reactor absorption characteristics at selected wavelengths. The charge distribution in the A-R, optimized for maximal temperature difference at 785 nm CW illumination, is shown in Figure 1c. The field enhancement in the antenna gap (at the edges of the reactor) is shown in Figure 1d. Theoretically, this design facilitates a substrate temperature closer to ambient while the reactor temperature increases by >70 °C when illuminated with a continuous 785 nm wavelength and ~435 kW/cm² laser intensity (Figure 1e).

The A-R structure was fabricated on top of a thermally grown 90 nm silica layer on a p-type doped Si substrate (Figure 2a; see Supporting Information for details). An ~200 nm PMMA coating was then applied (Figure 2b). The bowtie antenna pattern was exposed with electron beam lithography and developed (Figure 2c). The silica layer in the regions of the bowtie nanostructures was then removed with reactive ion etching (Figure 2d). A thin layer of 2 nm Ti, followed by 150 nm Au, was evaporated into the etched silica layer (Figure 2e), followed by lift-off, ensuring removal of excess Au (Figure 2f). A layer of PMMA was subsequently spin-coated onto the substrate (Figure 2g). The nanorod reactor pattern was then exposed with electron beam lithography, aligned with the gaps between the bowtie antennas and developed (Figure 2h). A thin layer of 10 nm Au was evaporated in the exposed nanorod gap (Figure 2i), followed by lift-off (Figure 2j). The evaporation produced structures with wall angles of ~83° utilized in all experimental simulations (see Figures S4 and S5).

To probe the local temperature at the reactor within the A-R structure, we performed nanothermometry measurements based on SERS. ^{31,32} The ratio of the Stokes and anti-Stokes intensities for strong Raman modes of an adsorbate molecule can be used to calculate the temperature of the molecules within the hotspots of a plasmonic nanostructure complex. ^{31–36} In our case, the well-defined gap region can be reliably used to determine the local temperature of the probe molecules sitting within the gap. Since the SERS signal scales as |E|⁴ of the local

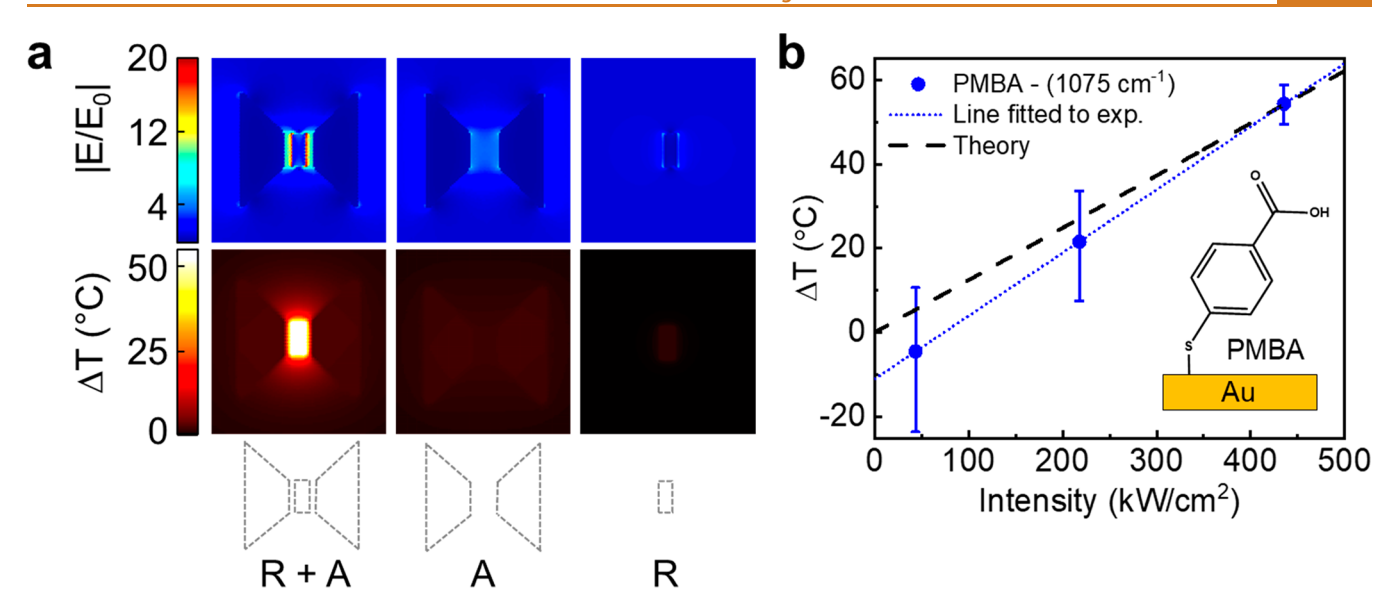


Figure 3. Nanothermometry of Au bowtie nanoheaters using SERS. (a) Calculated field enhancement and temperature increase in the individual nanorod reactor with antenna, just antenna, and just nanorod reactor. The field enhancement is shown at 785 nm illumination wavelength, and the temperature increase is shown at maximum laser illumination intensity of \sim 435 kW/cm². (b) Measured temperature increases for pMBA on Au bowtie nanoheaters (blue). The dashed black line represents the calculated temperature increase on the surface of the nanorod. Inset: schematic of how the pMBA molecules bind to the Au substrate.

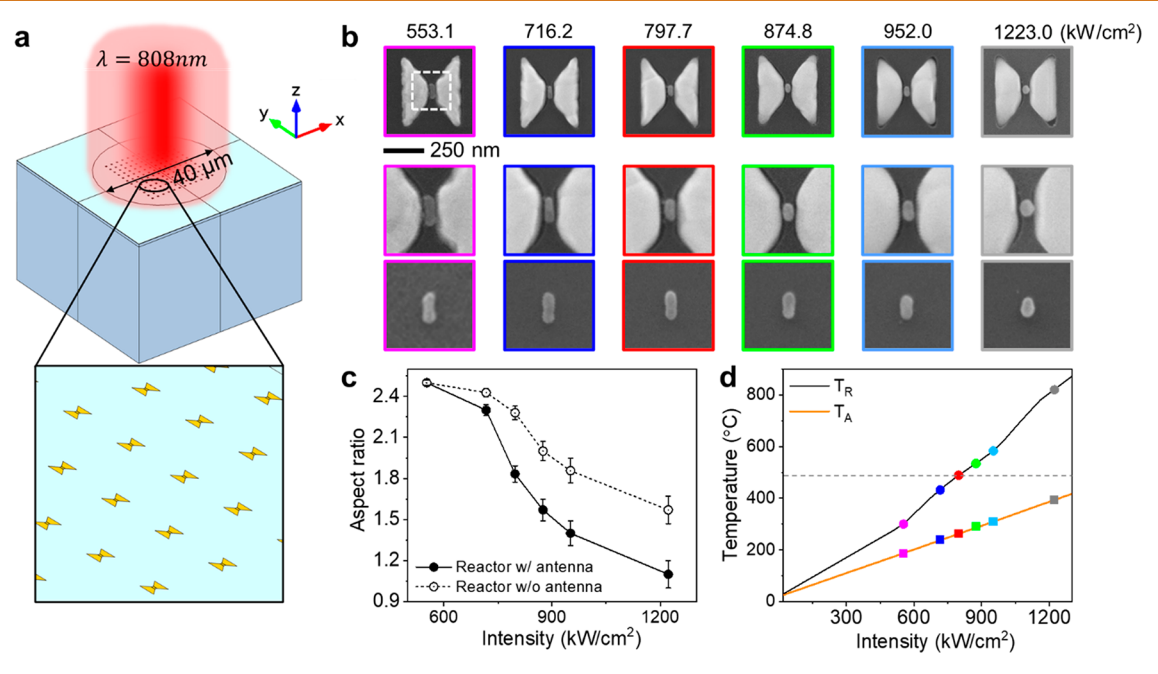


Figure 4. Experimental reshaping of the reactor with illumination. (a) Schematic showing the illumination of an array of A-R structures. (b) SEM images of the reactor with antenna illuminated at different laser intensities. The scale bar is 250 nm. Magnified insets (white dashed box) of the SEM images with SEM images of the reactors without antenna illuminated at the same intensities are shown in the following rows, respectively. (c) Change in the aspect ratio of the nanorod reactor with (solid black line) and without (dashed black line) surrounding antenna at different illumination laser intensities. (d) Simulated temperature increases in the reactor (T_R) , black solid line), antenna (T_A) orange solid line) in the combined A-R structure with laser illumination intensity. Temperatures corresponding to experiments are marked with solid symbols corresponding to the border colors in (b) for different illumination intensities. Melting temperature observed from furnace heating is shown with the gray dashed line. The light source is an 808 nm CW laser with illumination spot size of \sim 40 μ m.

field, only the molecules within the regions of the enhanced field will serve as reporters, providing quantifiable experimental validation of localized heating within the junction of the A-R structure.

The A-R structures designed and fabricated for optimized heating at the Raman pump laser wavelength of 785 were used (Figure 3a). The structures were plasma cleaned, then

functionalized with pMBA (see Supporting Information for details). We chose pMBA as the probe molecule for SERS nanothermometry since it strongly binds to Au through the Au—S bond and is known to form well-ordered self-assembled monolayers (SAMs).³⁷ Additionally, pMBA has several vibrational modes with a large Raman cross section, making detection more feasible, especially in the anti-Stokes region where

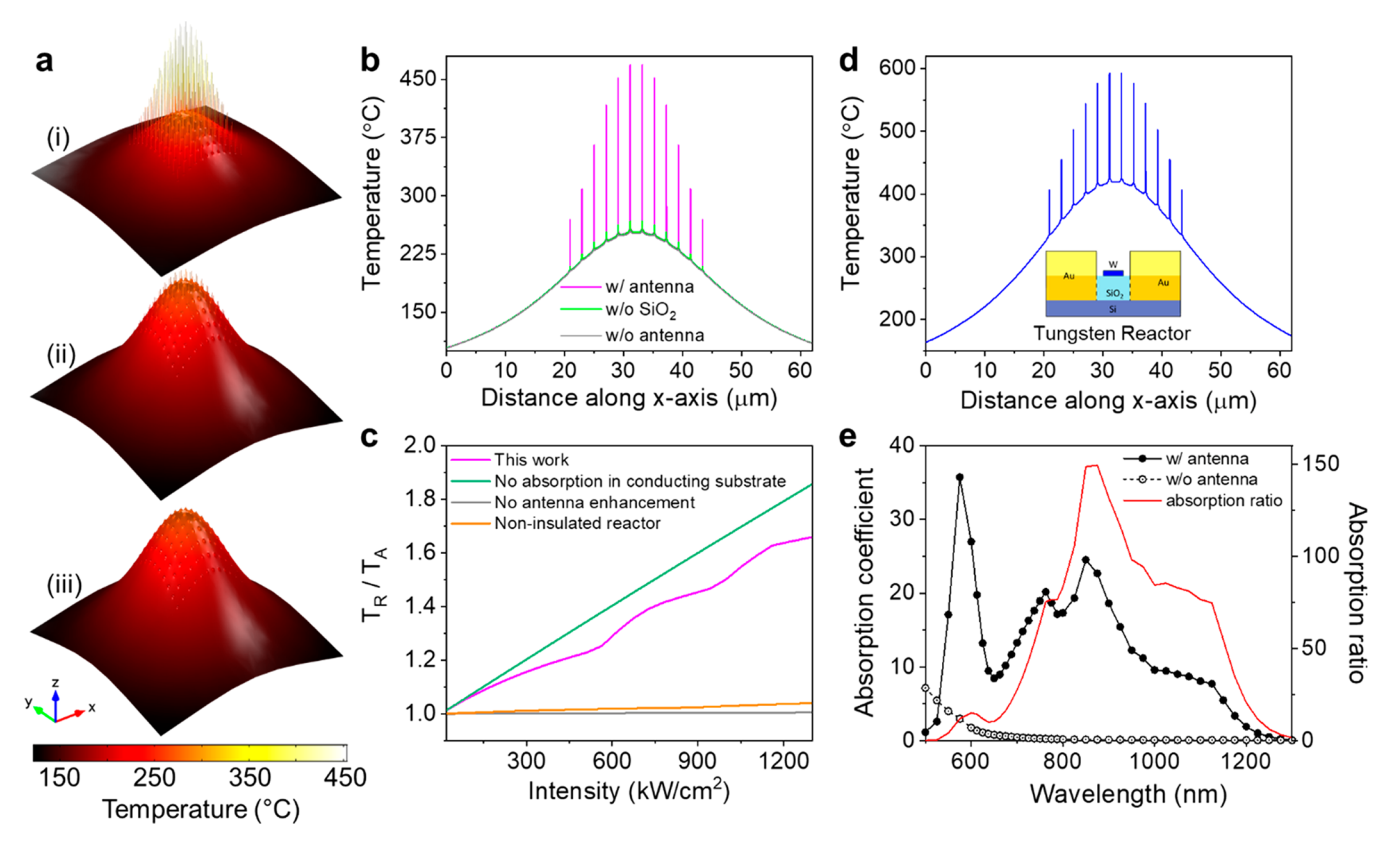


Figure 5. A-R array thermal calculations. (a) Simulated three-dimensional temperature profile of the complete system for an incident intensity of 771.3 kW/cm² (corresponding to 3.5 W power) for: current experimental setup (top), the case where the silica insulator between the reactor and the Si substrate is replaced by Si (middle), and the case where no antenna enhancement is considered, and reactors only are illuminated (bottom). (b) Temperature profiles for the cases in (a) along a horizontal line in the XY plane passing through the whole system at the reactor Z coordinate (see inset). Current work (magenta), noninsulated reactor (green), and no antenna enhancement (gray) cases are compared. (c) Ratio between the temperature of the reactor (T_R) and antenna (T_A) depending on incident intensity for different cases: current work setup (magenta), no antenna enhancement (gray), no absorption in the Si substrate where Si thermal conductivity was reduced to the silica one (light orange), and no absorption in the Si substrate. (d) Temperature profile similar to (b) in the case of tungsten reactors for an input intensity of 1322.2 kW/cm² (corresponding to 6 W power). (e) Left axis: reactor absorption cross section spectra for an array of W reactors only (red), an array of Au antennas and W reactors. Right axis: ratio between W reactors absorption cross section spectra in the case with and without Au antennas. In array simulations, a 12 × 12 array of A-R structures distanced 1.5 μ m are heated consistently with the calculated electromagnetic dissipation at a wavelength of 808 nm. Substrate heating in Si and silica within the 40 μ m diameter beam spot is accounted for through the materials absorption coefficients of 770 and 201 cm⁻¹, respectively.

intensities are inherently low. We focused our analysis on the strong Raman peak of pMBA at 1075 cm $^{-1}$, corresponding to the aromatic $\nu(CC)$ ring-breathing mode 37 (Figure S6). After functionalization, we measured the Stokes (I_{Stokes}) and anti-Stokes ($I_{\text{anti-Stokes}}$) Raman scattering from the Au bowties as a function of laser intensity (Figure S7). The laser intensity was controlled by using the built-in neutral density filters on the Renishaw Raman microscope, corresponding to 43.6, 217.8, and 435.5 kW/cm², corresponding to 10%, 50%, and 100% of the laser intensity (see details of our measurements and analysis in the Supporting Information). The temperature increases obtained experimentally for the three laser intensities were -4.4 ± 19.0 , 21.6 \pm 14, and 54.3 \pm 4.8 °C, respectively (Figure 3b). The temperature analysis error is greatest for the lowest intensity due to the low signal-to-noise of the anti-Stokes signal at this laser intensity range. The inherently low intensity of the anti-Stokes process, relatively large hotspot gap, and low number of probed structures result in an extremely low signal-to-noise ratio at low laser intensity. More details on the estimation of the error can be found in the Supporting Information. To further prove that the PMBA signal originated from the reactor structure within the A-R gap region and not from the antenna,

SERS measurements were obtained on antenna-only structures and polarized along the transverse axis of the A-R structure (Figure S8). When the incident polarization was in the transverse direction, no SERS signal from pMBA was observed. A small SERS signal from the antenna-only structure was due to the much larger gap dimension (~50 nm), but no anti-Stokes mode was observable (Figure S7). Additionally, we did not observe any pMBA signal from the Si substrate, even at the highest intensity. These additional control measurements show that the pMBA SERS signal originated from molecules adsorbed into the ~5 nm gap on each side of the reactor nanorod structure (Figure S8 and Figure 3a). A similar nanothermometry analysis was also performed on the amorphous silica peak appearing as an asymmetric peak between 910 and 1000 cm⁻¹ to determine the average temperature of the interlayer silica substrate illuminated by the laser spot (Figure S7c). The temperatures obtained using the silica SERS data revealed that the substrate heats only by a small amount, 4.3 \pm 10.3, 2.9 \pm 4.4, and 7.3 \pm 1.4 °C with increasing laser intensity (Figure S7c).

A theoretical model was developed to predict the temperature increase at the reactor site (details of these calculations are provided in the Supporting Information). The experimental

temperature determined from the SERS measurements agrees well with the calculated temperature increase at the nanoreactor, providing evidence that the bowtie antenna can efficiently generate quantifiable local heating on the nanorod reactor (Figure 3b).

In addition to investigating the localized temperature increases within an individually illuminated A-R structure, we extended our studies to A-R arrays. In light-driven nonlinear processes like solar-driven desalination³⁸ or photocatalysis, large arrays of localized, high-temperature hotspots could significantly enhance thermally driven processes compared to homogeneous temperature distributions.

The A-R array experiments were performed with a continuous wave (CW) laser at 808 nm (Diomed). The experimental setup is shown in Figure 4a. The distance between adjacent A-R nanostructures is 1.5 μ m. The beam waist of the laser spot size at the sample is \sim 40 μm (measured with a Thorlabs beam profilometer). The temperature generated in the nanorod reactors (T_R) under array illumination was monitored indirectly by assessing their reshaping with increasing laser intensity. Although the bulk Au melting temperature is 1064 °C, it is wellknown that the melting temperature of Au nanostructures is significantly depressed relative to their bulk value. 39-41 Heating in a conventional laboratory furnace was used to obtain the nanorod reactors' melting point. The reshaping of the nanorods at different temperatures and the corresponding change in the geometric aspect ratio is shown in Figure S9. When the A-R nanostructure is illuminated with the CW laser, a reshaping of the nanorod with varying laser power and intensity is observed (Figure 4). The reshaping occurs at lower incident laser intensities for a nanorod reactor within an antenna than for a bare nanorod without an antenna (Figure 4b). The presence of the antennas clearly enhances the optical absorption at 808 nm, increasing the temperature of the nanorod reactors in the antenna gaps. The distribution of energy flux represented by the Poynting vectors visually explains this effect (Figure S10). The antennas reshape at higher intensities than the nanorod reactors, most likely because the antennas are fabricated on the underlying doped Si substrate that promotes heat dissipation (Figure 4b). Higher temperature generation in nanorods with antennas compared to bare nanorods is evident from the observed higher change in aspect ratio with illumination intensity (Figure 4c). Three-dimensional simulations of A-R arrays show that the antenna temperature (T_A) is nominally 200 °C lower than the reactor temperature at 880 kW/cm² incident intensity (Figure 4d). The nonlinear trend of $T_{\rm R}$ is due to the temperature dependence of the Au permittivity, ⁴² which has been shown to affect the photothermal response of nanostructures across wide temperature ranges. 43,44

CONCLUSIONS

Our design strategy for nanostructures featuring large thermal gradients is to generate an imbalance in heat loss by thermally isolating the reactor while coupling the antenna to a heat sink. This approach achieves a non-homogeneous temperature profile over a larger area despite the collective heating effects induced by an array of nanostructures and intrinsic substrate dissipation (Figure 5). To account for all relevant thermal aspects of our system, we have modeled a realistic 12 \times 12 array of A-R structures, with a 1.5 μ m periodicity and an illumination diameter of \sim 40 μ m, consistent with the system used in the reshaping experiments (Figure 4a). The heat dissipation density applied to each antenna and reactor of the array is derived from

electromagnetic simulations (see Supporting Information). Additional dissipation from both the silica and Si substrate layers is also taken into account through their absorption coefficients (770 cm⁻¹⁴⁵ and 201 cm^{-1,46} respectively) at the illumination wavelength. In Figure 5a, we show the 3D temperature profile of the array when illuminated at ~3.5 W in three different variations: our experimental case (top), the case where the reactor is "short-circuited" to the Si substrate by substituting its silica underlayer with Si (middle), and the case where there is no antenna structure (bottom). The temperature maps clearly show how both the silica insulating layer beneath each reactor and the antenna absorption enhancement play critical roles in generating the localized temperature increases at the reactor sites. The temperature profiles along a line crossing a central row of the array at the reactor height are shown in Figure 5b for the same three cases as in Figure 5a. For all cases, the substrate temperature is similar and mostly due to the intrinsic absorption in the Si substrate (green). When both reactor insulation and antenna-driven absorption enhancement are in place, the temperature at the reactors is consistently at least 100 °C higher.

The temperature difference between reactor and antenna in A-Rs becomes important, for example, in the case of photothermal catalytic reactions whose reaction rates follow an Arrhenius temperature dependence $\propto \exp[-\gamma/T]$. For this case, it is crucial to quantify, in addition to reactor temperatures, their temperature values relative to nearby antennas. Hence, we define the ratio between reactor (T_R) and antennas (T_A) temperatures, T_R/T_A , as an additional figure of merit. We plot $T_{\rm R}/T_{\rm A}$ for increasing incident illumination intensities in Figure 5c by comparing our system (magenta) with other significant cases. The case where the antenna enhancement is neglected (gray) clearly shows how T_R/T_A approaches 1, meaning that there is no relevant temperature increase of the reactor with respect to the antenna and, thus, no temperature localization. The case where the Si substrate is substituted by a transparent, though insulating, material (light orange) shows that temperature localization improves only slightly, but T_R/T_A does not go past \sim 1.1 at even the highest simulated intensities. Our design at 3.5 W, instead, reaches values up to 1.5 (magenta), meaning that reactors can be up to ~50% hotter than the antennas, which are only \sim 5–10 nm away. For comparison, the rather idealistic case where the substrate does not absorb light and is also thermally conductive (Si thermal conductivity is assumed) is shown as a green line and reaches a maximum T_R/T_A of ~1.8. This study confirms the promising performance of our three-dimensional

Our approach can be extended in a straightforward manner to other reactor materials, which could be used to catalyze chemical reactions and would be able to sustain higher temperatures. To illustrate this application, we use the same geometry but substitute the Au reactor with a tungsten reactor. The calculated temperature profile is shown in Figure 5d for a power illumination of 6 W. The reactor temperatures can here be as high as ~640 °C, well below the W bulk melting temperature of \sim 3400 °C, while the antenna remains below \sim 420 °C. The absorption enhancement exceeds 100 for a relatively broad range of wavelengths (Figure 5e). We note that tungsten is metallic (negative electric permittivity) at our operational wavelength (808 nm) according to Werner et al.47 However, other works 48 have reported positive permittivity in the same wavelength range. We highlight the fact that our design significantly increases the reactor absorption for both choices

of tungsten permittivities (see Figure S12), further demonstrating how our A-R concept can be even applied to non-metallic materials.

In conclusion, the design and demonstration of this threedimensional plasmonic "nanoheater" demonstrates that one can establish sizable temperature gradients over ultrasmall length scales. This strategy is one of very general importance and provides a way to control temperatures for applications in research, such as spectroscopy and photocatalysis, and the study of physical processes at the nanoscale, such as phase transitions. Achieving nanoscale thermal hotspots and gradients in large arrays will also be useful in applications, such as solar energy harvesting and other light-driven processes, where the efficiencies follow Arrhenius-like laws.

MATERIALS AND METHODS

Antenna-Reactor Nanofabrication. The bowtie antenna-nanorod reactor structure is fabricated on top of a thermally grown 90 nm silica on a p-type doped Si substrate (thickness 525 μ m, resistivity 0.001-0.005 ohm-cm). The substrate was cleaned by sonication in acetone, followed by sonication in isopropyl alcohol (IPA) for 5 min each. It was then plasma-cleaned in argon plasma at a pressure of 0.85 bar for 3 min at 200 W power. Poly(methyl methacrylate) (PMMA) 950 A4 was spin-coated at 3000 rpm onto the cleaned substrate, resulting in a PMMA coating thickness of ~200 nm. The bowtie antenna pattern was then exposed with electron beam lithography. The resist was then developed in 1:3 methyl-isobutyl ketone (MIBK):IPA. The layer of 90 nm silica in the regions of developed bowtie nanostructures was then etched with reactive ion etching in a CHF3 and O₂ environment. A thin layer of 2 nm titanium, followed by 150 nm Au, was then evaporated into the etched silica layer. The lift-off was performed using 1-methyl-2-pyrrolidinone at 65 °C overnight to ensure removal of excess Au. A layer of ~70 nm PMMA 950 A2 was then spincoated onto the substrate to prepare for the second step of lithography. The nanorod reactor pattern was again exposed with electron beam lithography aligned with the gaps between the bowtie antennas fabricated earlier. The exposed resist was then developed in 1:3 MIBK:IPA. A thin layer of 10 nm Au was evaporated in the exposed nanorod gap. The lift-off of excess Au was carried out in 1-methyl-2pyrrolidinone at 65 °C for 1 h.

SERS Sample Preparation. Au bowtie antennas were first plasmacleaned to remove surface impurities following the fabrication procedure. The samples were then immersed in 1 mM *p*-mercaptobenzoic acid (pMBA) in 200 proof ethanol for 18–24 h at room temperature to ensure adequate binding. Samples were then rinsed thoroughly with 200 proof ethanol and dried under a stream of nitrogen gas.

ASSOCIATED CONTENT

Supporting Information

The Supporting Information is available free of charge at https://pubs.acs.org/doi/10.1021/acsnano.1c01046.

Detailed information on the dimensions of the antennareactor (A-R) structures, detailed nanofabrication protocols, experimental and theoretical darkfield scattering spectra for the fabricated structures, simulated temperatures and absorption in the A-R structures, surface enhanced Raman measurements, SERS nanothermometry, nanorod reshaping experiments due to heating in a furnace, Poynting vector distributions for just reactor, just antenna and the A-R structure, and implementation of theoretical simulations (PDF)

AUTHOR INFORMATION

Corresponding Authors

Alessandro Alabastri — Department of Electrical and Computer Engineering, Laboratory for Nanophotonics, and Nanosystems Engineering Research Center for Nanotechnology-Enabled Water Treatment (NEWT), Rice University, Houston, Texas 77005, United States; orcid.org/0000-0001-6180-8052; Email: alessandro.alabastri@rice.edu

Peter Nordlander — Department of Electrical and Computer Engineering, Laboratory for Nanophotonics, Nanosystems Engineering Research Center for Nanotechnology-Enabled Water Treatment (NEWT), and Department of Physics and Astronomy, Rice University, Houston, Texas 77005, United States; orcid.org/0000-0002-1633-2937; Email: nordland@rice.edu

Naomi J. Halas — Department of Electrical and Computer Engineering, Laboratory for Nanophotonics, Nanosystems Engineering Research Center for Nanotechnology-Enabled Water Treatment (NEWT), Department of Physics and Astronomy, and Department of Chemistry, Rice University, Houston, Texas 77005, United States; orcid.org/0000-0002-8461-8494; Email: halas@rice.edu

Authors

Pratiksha D. Dongare — Department of Electrical and Computer Engineering, Laboratory for Nanophotonics, Nanosystems Engineering Research Center for Nanotechnology-Enabled Water Treatment (NEWT), and Applied Physics Graduate Program, Rice University, Houston, Texas 77005, United States; orcid.org/0000-0003-0224-8109

Yage Zhao — Laboratory for Nanophotonics, Applied Physics Graduate Program, and Department of Physics and Astronomy, Rice University, Houston, Texas 77005, United States

David Renard – Laboratory for Nanophotonics and Department of Chemistry, Rice University, Houston, Texas 77005, United States

Jian Yang — Department of Electrical and Computer Engineering, Laboratory for Nanophotonics, and Applied Physics Graduate Program, Rice University, Houston, Texas 77005, United States

Oara Neumann – Department of Electrical and Computer Engineering, Laboratory for Nanophotonics, Nanosystems Engineering Research Center for Nanotechnology-Enabled Water Treatment (NEWT), and Applied Physics Graduate Program, Rice University, Houston, Texas 77005, United States

Jordin Metz – Nanosystems Engineering Research Center for Nanotechnology-Enabled Water Treatment (NEWT) and Department of Chemistry, Rice University, Houston, Texas 77005, United States

Lin Yuan – Laboratory for Nanophotonics and Department of Chemistry, Rice University, Houston, Texas 77005, United States

Complete contact information is available at: https://pubs.acs.org/10.1021/acsnano.1c01046

Author Contributions

P.D.D. fabricated samples and conducted array experiments. D.R. conducted the SERS experiments. Y.Z. performed theoretical simulations. O.N. and J.M. assisted in the experiments. L.Y. helped in conducting optical characterization. A.A.,

P.N., and N.J.H. oversaw the research. All authors discussed the results, and the manuscript was written through the contributions of all the authors.

Author Contributions

 $^{
abla}$ These authors contributed equally.

Notes

The authors declare no competing financial interest.

ACKNOWLEDGMENTS

This work was funded by the Nanoscale Science and Engineering Initiative of the NSF under NSF Award EEC-1449500, the Partnership for Innovation initiative of the NSF under award PFI: IIP 1941227, the Air Force Office of Scientific Research Grant FA9550-15-1-0022, and the Robert A. Welch Foundation Grants C-1220 (N.J.H.) and C-1222 (P.N.). Support for O.N. was provided through the Peter M. and Ruth L. Nicholas Fellowship and the Carl and Lillian Illig Fellowship. The authors also gratefully acknowledge help and support from the nanofabrication facility at the University of Houston for reactive ion etching.

REFERENCES

- (1) Jain, P. K.; Huang, X. H.; El-Sayed, I. H.; El-Sayed, M. A. Noble Metals on the Nanoscale: Optical and Photothermal Properties and Some Applications in Imaging, Sensing, Biology, and Medicine. *Acc. Chem. Res.* **2008**, *41* (12), 1578–1586.
- (2) Baffou, G.; Cichos, F.; Quidant, R. Applications and Challenges of Thermoplasmonics. *Nat. Mater.* **2020**, *19* (9), 946–958.
- (3) Neumann, O.; Urban, A. S.; Day, J.; Lal, S.; Nordlander, P.; Halas, N. J. Solar Vapor Generation Enabled by Nanoparticles. *ACS Nano* **2013**, 7 (1), 42–49.
- (4) Ghasemi, H.; Ni, G.; Marconnet, A. M.; Loomis, J.; Yerci, S.; Miljkovic, N.; Chen, G. Solar Steam Generation by Heat Localization. *Nat. Commun.* **2014**, *5* (1), 4449.
- (5) Rácz, P.; Pápa, Z.; Márton, I.; Budai, J.; Wróbel, P.; Stefaniuk, T.; Prietl, C.; Krenn, J. R.; Dombi, P. Measurement of Nanoplasmonic Field Enhancement with Ultrafast Photoemission. *Nano Lett.* **2017**, *17* (2), 1181–1186.
- (6) Ward, D. R.; Hüser, F.; Pauly, F.; Cuevas, J. C.; Natelson, D. Optical Rectification and Field Enhancement in a Plasmonic Nanogap. *Nat. Nanotechnol.* **2010**, *5* (10), 732–736.
- (7) Lalisse, A.; Tessier, G.; Plain, J.; Baffou, G. Quantifying the Efficiency of Plasmonic Materials for Near-Field Enhancement and Photothermal Conversion. *J. Phys. Chem. C* **2015**, *119* (45), 25518–25528.
- (8) Swearer, D. F.; Zhao, H. Q.; Zhou, L. N.; Zhang, C.; Robatjazi, H.; Martirez, J. M. P.; Krauter, C. M.; Yazdi, S.; McClain, M. J.; Ringe, E.; Carter, E. A.; Nordlander, P.; Halas, N. J. Heterometallic Antenna-Reactor Complexes for Photocatalysis. *Proc. Natl. Acad. Sci. U. S. A.* **2016**, *113* (32), 8916–8920.
- (9) Zhou, L.; Swearer, D. F.; Zhang, C.; Robatjazi, H.; Zhao, H.; Henderson, L.; Dong, L.; Christopher, P.; Carter, E. A.; Nordlander, P.; Halas, N. J. Quantifying Hot Carrier and Thermal Contributions in Plasmonic Photocatalysis. *Science* **2018**, *362* (6410), *69*.
- (10) Vampa, G.; Ghamsari, B. G.; Siadat Mousavi, S.; Hammond, T. J.; Olivieri, A.; Lisicka-Skrek, E.; Naumov, A. Y.; Villeneuve, D. M.; Staudte, A.; Berini, P.; Corkum, P. B. Plasmon-Enhanced High-Harmonic Generation from Silicon. *Nat. Phys.* **2017**, *13* (7), 659–662.
- (11) Cox, J. D.; Marini, A.; de Abajo, F. J. G. Plasmon-Assisted High-Harmonic Generation in Graphene. *Nat. Commun.* **2017**, 8 (1), 14380.
- (12) Han, S.; Kim, H.; Kim, Y. W.; Kim, Y.-J.; Kim, S.; Park, I.-Y.; Kim, S.-W. High-Harmonic Generation by Field Enhanced Femtosecond Pulses in Metal-Sapphire Nanostructure. *Nat. Commun.* **2016**, *7* (1), 13105.
- (13) Farmakidis, N.; Youngblood, N.; Li, X.; Tan, J.; Swett, J. L.; Cheng, Z.; Wright, C. D.; Pernice, W. H. P.; Bhaskaran, H. Plasmonic

- Nanogap Enhanced Phase-Change Devices with Dual Electrical-Optical Functionality. *Sci. Adv.* **2019**, *5* (11), No. eaaw2687.
- (14) Chen, W.-Y.; Lin, C.-H.; Chen, W.-T. Plasmonic Phase Transition and Phase Retardation: Essential Optical Characteristics of Localized Surface Plasmon Resonance. *Nanoscale* **2013**, *5* (20), 9950–9956.
- (15) Baffou, G.; Polleux, J.; Rigneault, H.; Monneret, S. Super-Heating and Micro-Bubble Generation around Plasmonic Nanoparticles under Cw Illumination. *J. Phys. Chem. C* **2014**, *118* (9), 4890–4898.
- (16) Baffou, G.; Berto, P.; Bermúdez Ureña, E.; Quidant, R.; Monneret, S.; Polleux, J.; Rigneault, H. Photoinduced Heating of Nanoparticle Arrays. *ACS Nano* **2013**, *7* (8), 6478–6488.
- (17) Baldwin, C. L.; Bigelow, N. W.; Masiello, D. J. Thermal Signatures of Plasmonic Fano Interferences: Toward the Achievement of Nanolocalized Temperature Manipulation. *J. Phys. Chem. Lett.* **2014**, 5 (8), 1347–1354.
- (18) Khosravi Khorashad, L.; Besteiro, L. V.; Wang, Z.; Valentine, J.; Govorov, A. O. Localization of Excess Temperature Using Plasmonic Hot Spots in Metal Nanostructures: Combining Nano-Optical Antennas with the Fano Effect. *J. Phys. Chem. C* **2016**, *120* (24), 13215–13226.
- (19) Bhattacharjee, U.; West, C. A.; Hosseini Jebeli, S. A.; Goldwyn, H. J.; Kong, X.-T.; Hu, Z.; Beutler, E. K.; Chang, W.-S.; Willets, K. A.; Link, S.; Masiello, D. J. Active Far-Field Control of the Thermal Near-Field *via* Plasmon Hybridization. *ACS Nano* **2019**, *13* (8), 9655–9663.
- (20) Naik, G. V.; Kim, J.; Boltasseva, A. Oxides and Nitrides as Alternative Plasmonic Materials in the Optical Range [Invited]. *Opt. Mater. Express* **2011**, *1* (6), 1090–1099.
- (21) Dao, T. D.; Hoang, C. V.; Nishio, N.; Yamamoto, N.; Ohi, A.; Nabatame, T.; Aono, M.; Nagao, T. Dark-Field Scattering and Local SERS Mapping from Plasmonic Aluminum Bowtie Antenna Array. *Micromachines* **2019**, *10* (7), 468.
- (22) Bharadwaj, P.; Deutsch, B.; Novotny, L. Optical Antennas. *Adv. Opt. Photonics* **2009**, *1* (3), 438–483.
- (23) Chirumamilla, M.; Toma, A.; Gopalakrishnan, A.; Das, G.; Zaccaria, R. P.; Krahne, R.; Rondanina, E.; Leoncini, M.; Liberale, C.; De Angelis, F.; Di Fabrizio, E. 3D Nanostar Dimers with a Sub-10-Nm Gap for Single-/Few-Molecule Surface-Enhanced Raman Scattering. *Adv. Mater.* **2014**, *26* (15), 2353–2358.
- (24) Juan, M. L.; Righini, M.; Quidant, R. Plasmon Nano-Optical Tweezers. *Nat. Photonics* **2011**, *5* (6), 349–356.
- (25) Liu, N.; Tang, M. L.; Hentschel, M.; Giessen, H.; Alivisatos, A. P. Nanoantenna-Enhanced Gas Sensing in a Single Tailored Nanofocus. *Nat. Mater.* **2011**, *10* (8), 631–636.
- (26) Roxworthy, B. J.; Ko, K. D.; Kumar, A.; Fung, K. H.; Chow, E. K. C.; Liu, G. L.; Fang, N. X.; Toussaint, K. C. Application of Plasmonic Bowtie Nanoantenna Arrays for Optical Trapping, Stacking, and Sorting. *Nano Lett.* **2012**, *12* (2), 796–801.
- (27) O'Connor, D.; Zayats, A. V. The Third Plasmonic Revolution. *Nat. Nanotechnol.* **2010**, *5* (7), 482–483.
- (28) Chen, H.; Bhuiya, A. M.; Ding, Q.; Toussaint, K. C. Plasmon-Assisted Audio Recording. Sci. Rep. 2015, 5 (1), 9125.
- (29) Mancini, A.; Giliberti, V.; Alabastri, A.; Calandrini, E.; De Angelis, F.; Garoli, D.; Ortolani, M. Thermoplasmonic Effect of Surface-Enhanced Infrared Absorption in Vertical Nanoantenna Arrays. *J. Phys. Chem. C* **2018**, *122* (24), 13072–13081.
- (30) Mancini, A.; Giliberti, V.; Alabastri, A.; Calandrini, E.; De Angelis, F.; Garoli, D.; Ortolani, M. Nanoscale Thermal Gradients Activated by Antenna-Enhanced Molecular Absorption in the Mid-Infrared. *Appl. Phys. Lett.* **2019**, *114* (2), 023105.
- (31) Kip, B. J.; Meier, R. J. Determination of the Local Temperature at a Sample during Raman Experiments Using Stokes and Anti-Stokes Raman Bands. *Appl. Spectrosc.* **1990**, *44* (4), 707–711.
- (32) Maher, R. C.; Cohen, L. F.; Gallop, J. C.; Le Ru, E. C.; Etchegoin, P. G. Temperature-Dependent Anti-Stokes/Stokes Ratios under Surface-Enhanced Raman Scattering Conditions. *J. Phys. Chem. B* **2006**, *110* (13), 6797–6803.

- (33) Brandt, N. C.; Keller, E. L.; Frontiera, R. R. Ultrafast Surface-Enhanced Raman Probing of the Role of Hot Electrons in Plasmon-Driven Chemistry. *J. Phys. Chem. Lett.* **2016**, *7* (16), 3179–3185.
- (34) Keller, E. L.; Frontiera, R. R. Ultrafast Nanoscale Raman Thermometry Proves Heating Is Not a Primary Mechanism for Plasmon-Driven Photocatalysis. ACS Nano 2018, 12 (6), 5848–5855.
- (35) Sarhan, R. M.; Koopman, W.; Schuetz, R.; Schmid, T.; Liebig, F.; Koetz, J.; Bargheer, M. The Importance of Plasmonic Heating for the Plasmon-Driven Photodimerization of 4-Nitrothiophenol. *Sci. Rep.* **2019**, 9 (1), 3060.
- (36) Pozzi, E. A.; Zrimsek, A. B.; Lethiec, C. M.; Schatz, G. C.; Hersam, M. C.; Van Duyne, R. P. Evaluating Single-Molecule Stokes and Anti-Stokes Sers for Nanoscale Thermometry. *J. Phys. Chem. C* **2015**, *119* (36), 21116–21124.
- (37) Michota, A.; Bukowska, J. Surface-Enhanced Raman Scattering (Sers) of 4-Mercaptobenzoic Acid on Silver and Gold Substrates. *J. Raman Spectrosc.* **2003**, 34 (1), 21–25.
- (38) Dongare, P. D.; Alabastri, A.; Neumann, O.; Nordlander, P.; Halas, N. J. Solar Thermal Desalination as a Nonlinear Optical Process. *Proc. Natl. Acad. Sci. U. S. A.* **2019**, *116* (27), 13182.
- (39) Chen, T.; Ma, Y.; Fu, X.; Li, M. A Comprehensive Understanding of the Melting Temperature of Nanocrystals: Implications for Catalysis. *ACS Appl. Nano Mater.* **2020**, 3 (2), 1583–1591.
- (40) Liu, Z. One-Step Fabrication of Crystalline Metal Nanostructures by Direct Nanoimprinting below Melting Temperatures. *Nat. Commun.* **2017**, 8 (1), 14910.
- (41) Puri, P.; Yang, V. Effect of Particle Size on Melting of Aluminum at Nano Scales. J. Phys. Chem. C 2007, 111 (32), 11776–11783.
- (42) Alabastri, A.; Tuccio, S.; Giugni, A.; Toma, A.; Liberale, C.; Das, G.; Angelis, F.; Fabrizio, E. D.; Zaccaria, R. P. Molding of Plasmonic Resonances in Metallic Nanostructures: Dependence of the Non-Linear Electric Permittivity on System Size and Temperature. *Materials* **2013**, *6* (11), 4879–4910.
- (43) Alabastri, A.; Malerba, M.; Calandrini, E.; Manjavacas, A.; De Angelis, F.; Toma, A.; Proietti Zaccaria, R. Controlling the Heat Dissipation in Temperature-Matched Plasmonic Nanostructures. *Nano Lett.* **2017**, *17* (9), \$472–\$480.
- (44) Alabastri, A.; Toma, A.; Malerba, M.; De Angelis, F.; Proietti Zaccaria, R. High Temperature Nanoplasmonics: The Key Role of Nonlinear Effects. *ACS Photonics* **2015**, 2 (1), 115–120.
- (45) Schinke, C.; Christian Peest, P.; Schmidt, J.; Brendel, R.; Bothe, K.; Vogt, M. R.; Kröger, I.; Winter, S.; Schirmacher, A.; Lim, S.; Nguyen, H. T.; MacDonald, D. Uncertainty Analysis for the Coefficient of Band-to-Band Absorption of Crystalline Silicon. *AIP Adv.* **2015**, *S* (6), 067168.
- (46) Rodríguez-de Marcos, L. V.; Larruquert, J. I.; Méndez, J. A.; Aznárez, J. A. Self-Consistent Optical Constants of Sio2 and Ta2o5 Films. *Opt. Mater. Express* **2016**, *6* (11), 3622–3637.
- (47) Werner, W. S. M.; Glantschnig, K.; Ambrosch-Draxl, C. Optical Constants and Inelastic Electron-Scattering Data for 17 Elemental Metals. *J. Phys. Chem. Ref. Data* **2009**, 38 (4), 1013–1092.
- (48) Lynch, D. W.; Hunter, W. R. Comments on the Optical Constants of Metals and an Introduction to the Data for Several Metals. In *Handbook of Optical Constants of Solids*; Palik, E. D., Ed.; Academic Press: Boston, 1985; pp 275–367.